Spatial variation of melt pool geometry, peak temperature and solidification parameters during laser assisted additive manufacturing process

V. Manvatkar, A. De and T. DebRoy*

A three-dimensional heat transfer and material flow model is developed to numerically simulate the temperature and velocity fields in a laser assisted layer by layer deposition process with coaxially fed powder particles. The computed results are tested with independently reported temperature and build geometry for the deposition of multilayered structures of austenitic stainless steel. The results provide detailed insight about the important physical processes and show that the model can be used to understand the effects of process parameters on the thermal cycles, build geometry, cooling rates and solidification parameters in a multilayer additive manufacturing process.

Keywords: Laser additive manufacturing, Multilayer deposition, Stainless steel, Heat transfer, 3D printing, Fluid flow

This paper is part of a special issue on Additive manufacturing

Introduction

Laser assisted additive manufacturing often involves melting and solidification of a stream of alloy powder that flows coaxially with a laser beam to form a component. The particles absorb energy from the laser beam as they traverse through the beam and subsequently get deposited into a small melt pool that forms directly under the laser beam. The laser beam rapidly moves forward and the solidification of the molten pool forms the component. Repeated traverse of the laser beam is required to form a multilayered structure. Interaction between the powder and the laser beam, small size of melt pool, high peak temperature and rapid solidification of the moving liquid pool make the real time process monitoring difficult. Fabrication of defect free and structurally sound components require precise control of many process variables such as the chemical composition, size distribution and flow rate of the powder particles, laser power, power density distribution and scanning speed.

Since many variables affect the microstructure and mechanical properties of the component in laser assisted multilayer additive manufacturing, their selection by trial and error is time consuming and expensive. A well tested comprehensive numerical model of heat transfer and material flow can be helpful in the selection of variables. In addition, a phenomenological model can provide valuable insight about the temperature fields, melt pool geometry and solidification parameters for understanding and controlling the microstructure and mechanical properties of the fabricated components.

The additive manufacturing process has shown considerable promise for the fabrication of components from titanium alloys,[1] nickel based super alloys,[2] stainless steel,[3–6] tool steel[6,7] and some ceramic materials.[8] Tests are underway to explore possible use of intermetallics,[9] metal matrix composites[10] and building functionally gradient structures.[11] However, the commercial adaptation of the process has been limited due to lack of understanding of the role of many process variables on the structure and properties of the products. Understanding of spatial and temporal variations of build geometry, temperature field, cooling rate and solidification parameters based on scientific principles can be helpful in expanding the commercial applications of the process.

One- and three-dimensional Conduction heat transfer models are used to analyse the laser assisted additive manufacturing.[3,12–15]Although these models estimated the evolution of melt pool geometry and build profile, the convective transport of heat in the melt pool was neglected in these models. As a result, the peak temperatures and the cooling rates were significantly overestimated.[13,15] Accurate calculations are important for the understanding of layerwise variations of the solidification structure and the mechanical properties. In the recent past, three-dimensional heat transfer and fluid flow models have been used to analyse a single layer laser cladding process.[16–18] Kong and Kovacevic[19] and Morville *et al.*[20] reported two-dimensional heat transfer and fluid flow models for laser assisted multilayered deposition of H13 tool steel and Ti6Al4V alloy structures respectively. These models used computationally intensive level set method[16–19] and arbitrary

The Pennsylvania State University, University Park, PA, USA

*Corresponding author, email debroy@matse.psu.edu

Published by Maney on behalf of the Institute
Received 9 September 2014; accepted 21 October 2014
DOI 10.1179/1743284714Y.0000000701

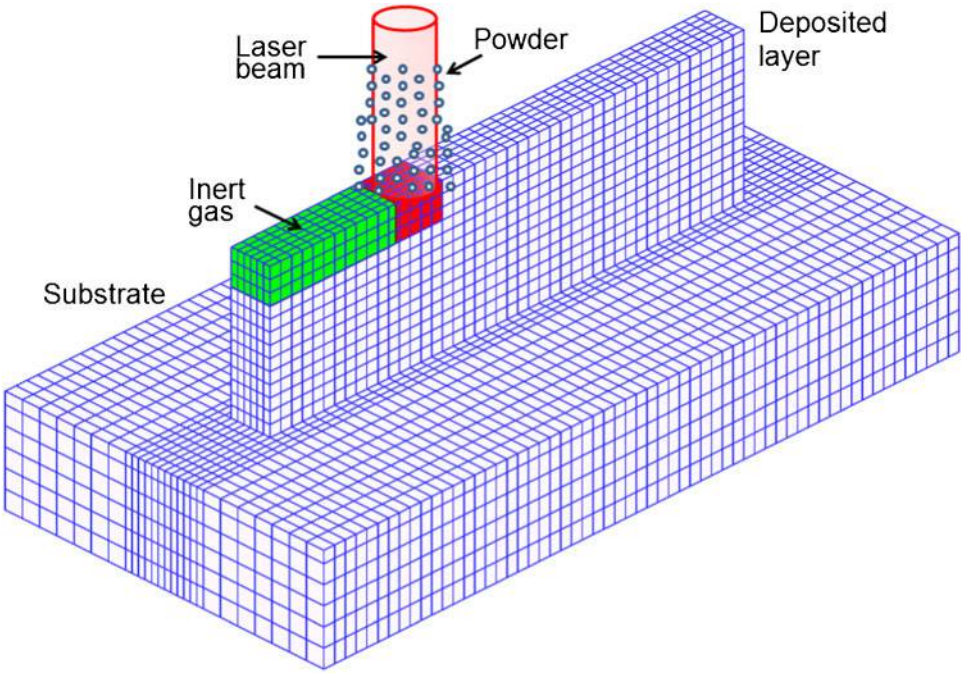

1 Solution domain showing feeding of powder particles through laser beam

Langrangian–Eulerian[20] moving mesh for the calculations. Raghavan *et al.*[21] adapted a computationally efficient three-dimensional heat transfer and fluid flow model for welding to examine the effect of process parameters on the melt pool geometry and solidification parameters in additive manufacturing. However, the addition of the powder was not explicitly considered in the model.

A computationally efficient three-dimensional heat transfer and fluid flow model that can consider the addition of powder particles and simulate the peak temperature, thermal cycles, build geometry and the solidification parameters in laser assisted multilayer additive manufacturing process is needed but not available in the literature. This need is addressed in this paper. The model solves the equations of conservation of mass, momentum and energy with appropriate boundary conditions and temperature dependent material properties. The absorption of laser beam energy by the powder particles as they pass coaxially through the beam is considered in the calculations. The computed results of build geometry, peak temperature and temperature profiles in the melt pool are validated with the corresponding independent experimentally measured results.

Numerical modelling

Equations of conservation of mass, momentum and energy are solved in transient three-dimensional form to calculate the temperature and velocity fields in laser assisted multilayer additive manufacturing. The process variables include the size distribution and mass flow rate of the powder particles, the in-flight length of the particles and the total power, power density distribution and the laser beam scanning speed.

The assumptions made in the model include a flat surface of the melt pool and constant densities of the solid and liquid alloy. The loss of alloying elements and the resulting compositional change owing to vaporisation are ignored in the calculations. The details of the governing equations and the boundary conditions are available in previous publications[21,22] and not repeated here.

The governing equations are discretised using the control volume method, where the computational domain shown in Fig. 1 is divided into small rectangular control volumes. At the beginning of the simulation, the computational volumes above the substrate are assigned the properties of an inert gas, e.g. argon. Following each shift of the laser beam, a set of discrete cells under the beam are filled up with powder materials and these computational volumes are assigned properties of the powder material. The time step for each discrete shift of the laser beam was calculated from the distance and the scanning speed. An idle time is considered at the end of the simulation of each layer. The deposition of a new layer is considered to start at the initial location on the top of the previous layer. The procedure is repeated until the simulation of all the layers is completed. The process parameters used for the calculations are listed in Table 1. Temperature dependent thermophysical properties[13,23–25] used in the model are presented in Table 2. The analysis is carried out for the deposition of a single line nine-layer structure of 316 stainless steel.

Table 1 Data used for numerical simulations

Process parameter	Value
Substrate size/mm × mm × mm	10 × 3·1 × 4
Deposited layer size/mm × mm × mm	4 × 0·72 × 0·38
Laser power/W	170–250
Laser scanning speed/mm s^{-1}	10–20
Laser beam diameter/mm	1·0
Idle time/s	0·5
Laser distribution factor	3
Material flowrate/gm min^{-1}	25
Material powder size/μm	175
Laser material interaction length/mm	2
Particle velocity/m s^{-1}	1·5
Carrier gas flowrate/L min^{-1}	4

The energy absorbed by the powder particles during flight and by the depositing layer is considered through a volumetric source term in the energy conservation equation as[26]

$$S_i = \frac{Pd}{\pi r_b^2 t}\left[\eta_p + (1-\eta_p)\eta_l\right]\exp\left(-d\frac{r^2}{r_b^2}\right) \quad (1)$$

where η_p is fraction of laser energy absorbed by the powder during flight, P is laser power, d is beam energy distribution factor, t is layer thickness, r_b is focused beam radius and r is radial distance from the beam axis. The first term within the bracket considers the fraction of laser beam energy transferred to the particles during their flight. The energy absorbed by the growing layer due to irradiation of the laser beam on the depositing surface is estimated by the second term within the bracket in equation (1). The term η_l refers to absorption coefficient of the growing layer. Initially, η_l has a high value for the solid powder particles but it decreases to Fresnel absorption coefficient when the powder melts. The exponential term outside the curly bracket accounts for the Gaussian distribution of laser energy. The beam diameter and the power distribution factor were taken from Ref. 15.

The fraction of laser beam energy transferred to the particles during their flight through the beam, η_p is calculated by estimating the temperature rise of the particles and their mass flow rate. The temperature rise of the particles as they travel through the laser beam is estimated using a heat balance as[26]

$$\Delta T = \frac{\eta_m \times \eta_s \times \left(P/\pi r_b^2\right) \times \left(2\pi r_p^2\right)\tau}{4/3 \times \pi \times r_p^3 \times C_p \times \rho_p} \quad (2)$$

where ΔT is the average in-flight temperature rise of the powder particles, P is the laser power, r_b and r_p are the laser beam radius and the average radius of the particles, respectively, C_P is the specific heat, η_m is an interference factor to account for shielding of some particles from the laser beam by other particles, η_s is the fraction of available laser power absorbed by the solid particles, τ is the time of flight which depends on the velocity of particles and the laser material interaction length and ρ_P is the density of the particles. The laser material interaction length is the distance between the point where particles are introduced into the laser beam and the deposition surface and is estimated from the geometry of the deposition system. Particle velocities were estimated using the mass flow rate of powder particles, the gas flow rate and the computed drag force of gas on the power particles as indicated in Ref. 25. For the experimental conditions considered, the powder particles did not melt after travelling though laser beam and were deposited on the moving liquid pool. The temperature of the powder particles at the end of their flight depends on their size, velocity, thermal properties and the power density of the laser beam. For the conditions considered here, 175 mm diameter particles were heated to 879 K. The fraction of laser beam energy transferred to the particles, η_p is estimated as[26]

$$\eta_p = \frac{\Delta T \times \dot{m} \times C_p}{P} \quad (3)$$

The initial temperature of the solution domain is considered to be 300 K. The spatial gradients of temperature and velocities are set to zero at the plane of symmetry.[21,27] The heat loss by convection and radiation are applied as boundary conditions on the remaining surfaces for the solution of enthalpy (temperature).[21,27] The velocities arising from the surface tension variation due to temperature gradient are applied at the top surface of the melt pool for the solution of momentum equations.[21,27] The discretised linear equations are solved following the tridiagonal matrix algorithm.[28] For each time step, convergence of the iterated values is evaluated based on the magnitudes of the residuals of enthalpy and three components of velocities.[21,27]

Results and discussion

Figures 2 shows the progressive growth of the melt pool at the mid-length of each layer in a nine-layer structure. The solidus contour represents the boundary of the melt pool indicating its shape and size. A continuous increase in the melt pool size is observed as the deposition progresses to upper layers. The velocity of the liquid in melt pool is represented by the black coloured arrows. The motion of the molten material within the melt pool is governed primarily by the Marangoni force owing to the variation in the surface tension at the melt pool surface due to spatial gradient of temperature.

Table 2 Material properties used for numerical simulations

Material properties	Values	Reference
Properties of SS316		
Density/kg mm^{-3}	7800	24
Solidus temperature/K	1693	24
Liquidus temperature/K	1733	24
Thermal conductivity/W m^{-1}/K^{-1}	$11{\cdot}82+0{\cdot}0106T$	24
Specific heat/J kg^{-1} K^{-1}	$330{\cdot}86+0{\cdot}563T-4{\cdot}015\times10^{-4}T^2+9{\cdot}465\times10^{-8}T^3$	24
Latent heat of fusion/J kg^{-1}	$2{\cdot}67\times10^5$	24
Coefficient of thermal expansion/K^{-1}	$1{\cdot}9\times10^{-5}$	24
Viscosity of liquid alloy/kg m^{-1} s^{-1}	$6{\cdot}7\times10^{-3}$	24
Temperature coefficient of surface tension/N m^{-1} K^{-1}	$-0{\cdot}4\times10^{-3}$	24
Laser absorption coefficient in loose powder form	0·28	23
Laser absorption coefficient for powder bed	0·7	23
Properties of argon		
Density/kg mm^{-3}	0·974	25
Specific heat/J kg^{-1} K^{-1}	520	25
Thermal conductivity/W m^{-1} K^{-1}	$26{\cdot}41\times10^{-3}$	25

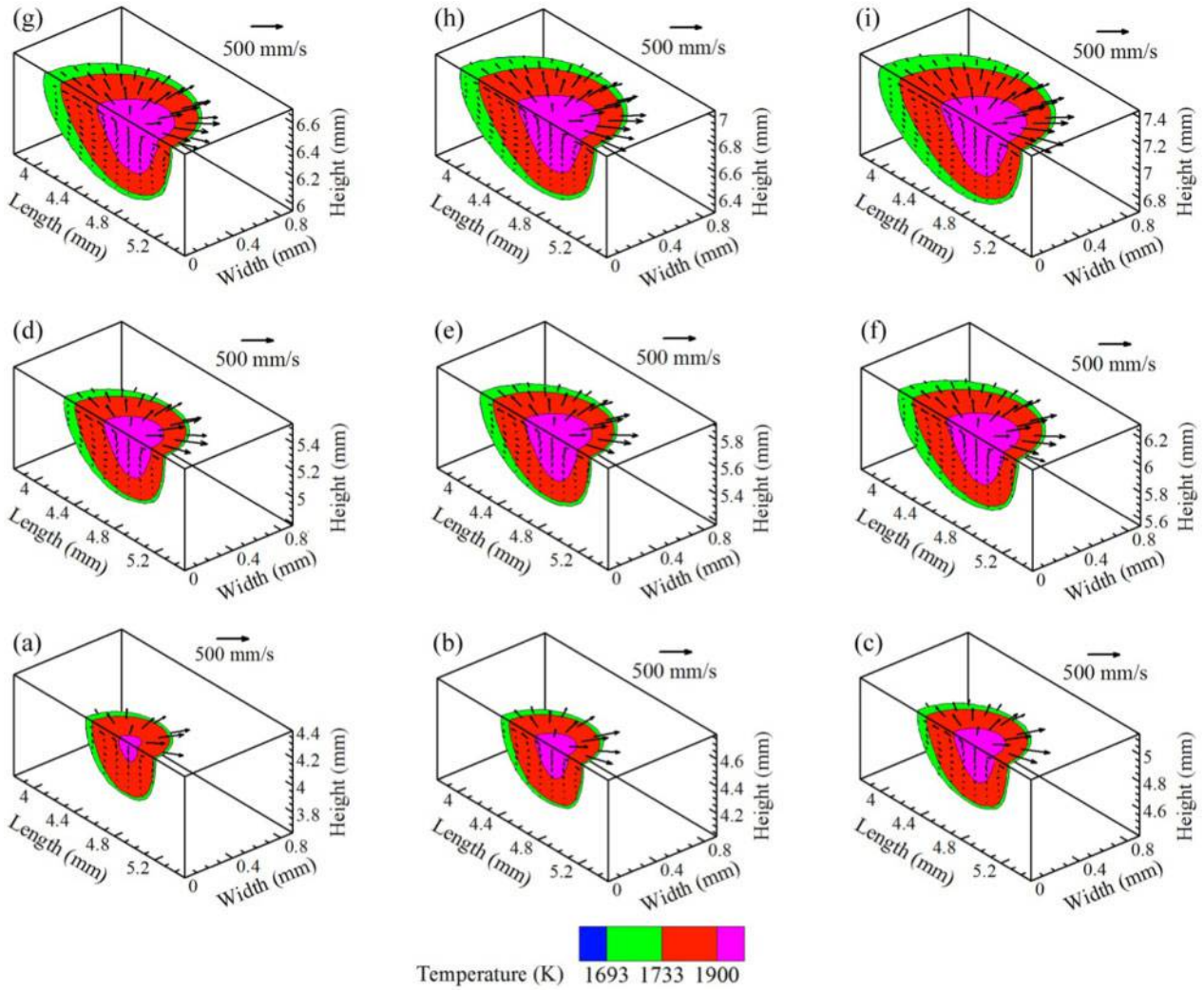

2 Computed melt pool shape, temperature and velocity fields in *a* first, *b* second, *c* third, *d* fourth, *e* fifth, *f* sixth, *g* seventh, *h* eighth and *i* ninth layers at mid-length for laser assisted multilayer deposition of 316 stainless steel powder particles at laser power of 210 W and scanning speed of 12·7 mm s^{-1}: figures are numbered from bottom to top to show progress of melt pool growth from first to ninth layer

The computed velocities in melt pool increase from approximately 400 mm s^{-1} in the first layer to 600 mm s^{-1} in the ninth layer. Velocities of similar magnitudes were also calculated by Qi *et al.*[16] and He and Mazumder.[17] The velocities ranging from several hundred mm s^{-1} to few m s^{-1} have been reported during laser welding.[29,30] At such high velocities, Pe, which is the ratio of the heat transfer by convection to that by conduction, is much higher than 1. This high value indicates that the convective transport is the main mechanism of heat transfer in the melt pool.

The transverse sections at the mid-length of the computed melt pools in each layer in a nine layer deposit are superimposed to depict the complete build profile in Fig. 3. The boundary of the experimentally measured[15] build profile is shown by a thick black line for clarity. A fair agreement between the computed and corresponding experimentally determined profile can be noted in Fig. 3. The increase in the melt pool dimensions towards top layers shown in Fig. 2 and 3 can be attributed to the reduced influence of substrate as a heat sink. The lower layers experience higher rate of heat extraction in comparison to the upper layers resulting in a variation of wall thickness from the lower to the upper layers. The flat top of the deposited structure originates from the rectangular fixed grids used for simplicity. The free surface of the liquid pool was not computed.

The computed temperature profiles are also tested against independent experimental results of Hofmeister *et al.*[3] using thermal imaging technique. Figure 4*a* shows a comparison of the numerically computed temperature profiles from the heat transfer and fluid flow model and the corresponding independent experimentally measured results.[3] Figure 4*a* also depicts the computed temperature profile obtained from a heat conduction based model.[13] The heat conduction calculations[13] show an overestimation of the peak temperature and a steep temperature gradient in the melt pool, since the mixing of the hot and the cold fluids is neglected when convection is ignored. In contrast, the computed temperature profile from the heat transfer and fluid flow model indicates a closer agreement with the experimentally measured temperature profile.[3] Figure 4*b* further shows a fair agreement between the computed peak temperatures from the heat transfer and fluid flow model and the corresponding experimentally measured results[3] in multilayer SS316 deposits at several laser powers. Increase in laser power increases the rate of heat input resulting in greater peak

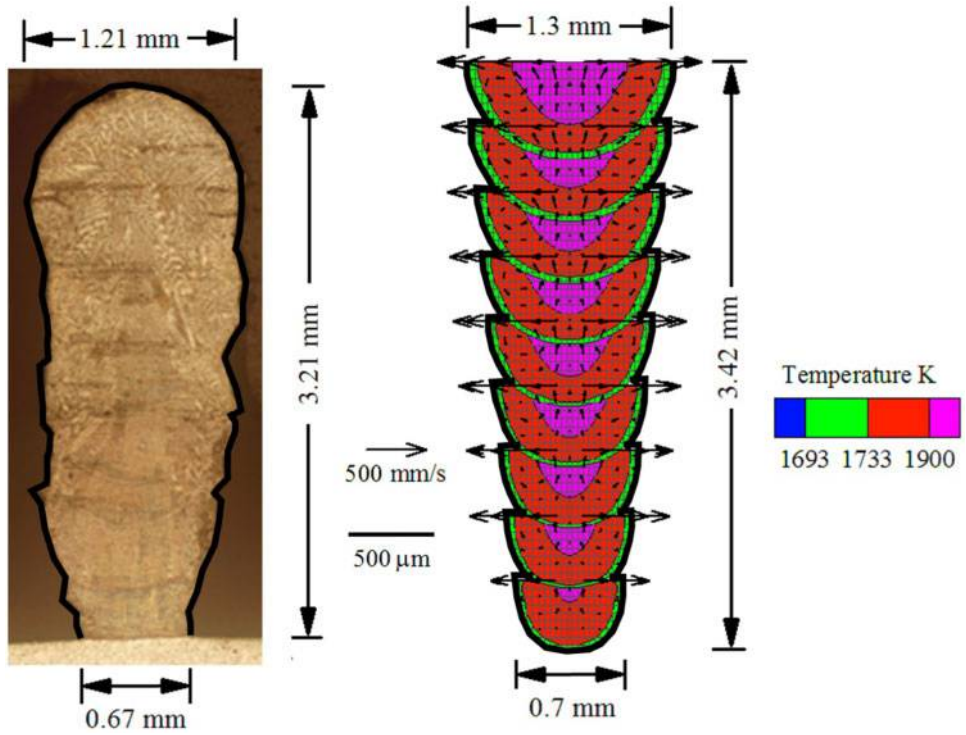

3 Experimentally measured[15] and corresponding computed build profile of nine-layer 316 stainless steel deposit at beam power of 210 W and scanning speed of 12·7 mm s^{-1}: both computed and measured profiles show transverse section at mid-length

temperature. The fair agreement between the computed results and the corresponding experimentally measured results in Figs. 3 and 4 shows the usefulness of the heat transfer and fluid flow model to simulate laser assisted multilayer additive manufacturing. The model is next used to examine the quantitative influence of the important process variables on the thermal cycles, cooling rates and solidification parameters.

Figure 5 presents the computed thermal cycles at the mid-height and mid-length of the alternate layers in a nine-layer structure. In each of these thermal cycles, the first temperature peak corresponds to a position of the laser beam just above the monitoring location and the subsequent peaks occur during the deposition of the upper layers. The peak temperature increases from 1878 K in the first layer to 1939, 1980, 2004 and 2020 K in the third, fifth, seventh and

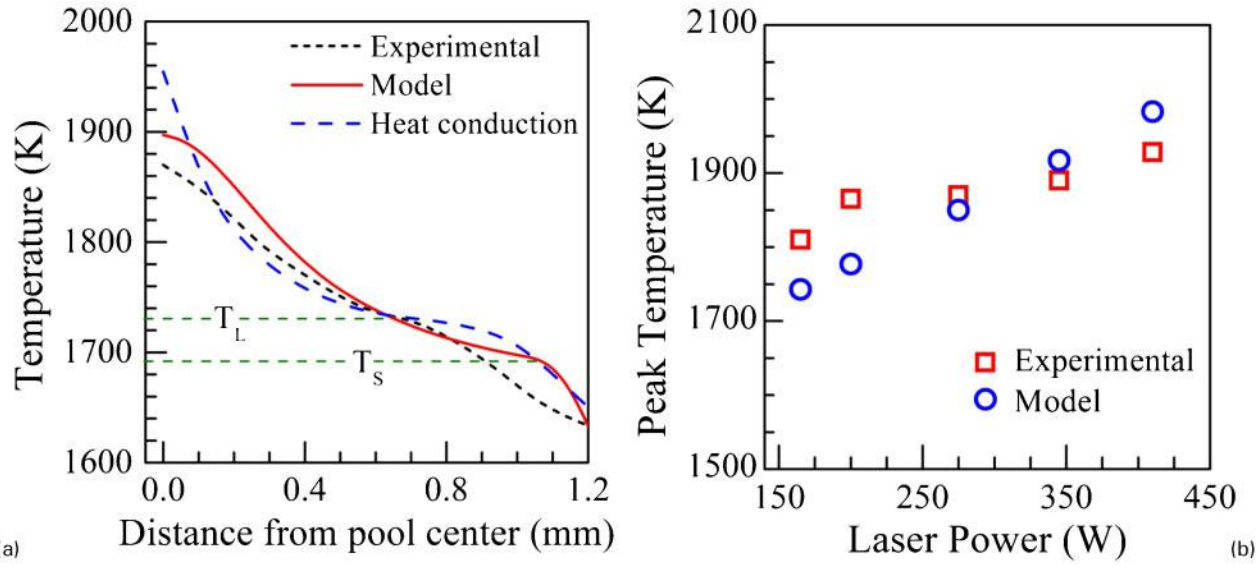

4 *a* comparison of experimentally measured[3] temperature profile and that computed using heat conduction based model[13] and heat transfer and fluid flow model in laser assisted multilayer deposit of SS316 at laser power of 275 W and scanning speed of 7·62 mm s^{-1}: T_L and T_S indicate the liquidus and solidus temperatures of 316 stainless steel respectively; presented temperature profile is plotted; *b* comparison of experimentally measured[3] and computed values of melt pool peak temperature in laser assisted multilayer deposit of SS316 at several laser powers at constant scanning speed of 7·62 mm s^{-1}

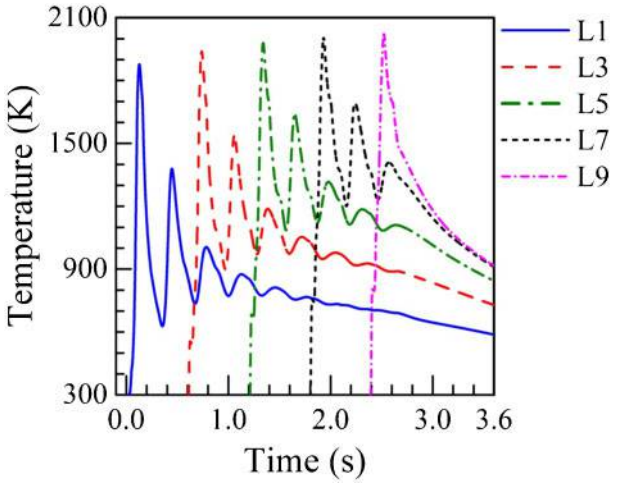

5 Computed thermal cycles in first (L1), third (L3), fifth (L5), seventh (L7) and ninth (L9) layers in laser assisted nine-layer deposition of 316 stainless steel at laser power of 210 W and scanning speed of 12·7 mm s^{-1}: monitoring locations for thermal cycles are at mid-length and mid-height of each layer

ninth layers respectively. As the deposition moves to the upper layers, the rate of heat loss through the substrate reduces resulting in greater peak temperatures.

Figure 6 shows the variations of cooling rate in the second, fifth and ninth layers as a function of beam scanning speed for two laser powers. The computed values of cooling rate during solidification decreases from 4997 K s^{-1} in the second layer to 2325 K s^{-1} in the fifth and 1001 K s^{-1} in the ninth layer. The continuous reduction in the cooling rate during solidification in the upper layers is attributed to the reduced rate of heat transfer to the substrate as the deposition moves to the top layers. The computed cooling rates at all locations increase significantly with increasing welding speed. For example, the computed cooling rate at a monitoring location at the mid-length and mid-height in the second layer increases from 4997 to 7395 K s^{-1} when the scanning speed is increased from 10 to 20 mm s^{-1}. Higher scanning speed results in steeper temperature gradient and higher cooling rates because of lower heat input per unit length. In contrast, the computed cooling rates at the same monitoring locations in the second layer decreases from 4997 to 4448 K s^{-1} when the laser power increases from 230 to 250 W. Increase in laser power at a constant scanning speed increases both the rate of heat input and the pool volume resulting in reduced cooling rate.

The ratio of the temperature gradient (G) and the growth rate (R) during solidification of the melt pool affect the morphology of the solidification structure. Figure 7 shows the computed values of G/R in the second, fifth and ninth layers as function of scanning speed for two laser powers. The computed value of G/R decreases from 50 K s mm^{-2} in the second layer to 10 K s mm^{-2} in the ninth layer. Similarly, an increase in the laser power from 230 to 250 W reduces the G/R ratio from 50 to 44 K s mm^{-2} in the second layer. This trend is attributable to the lower temperature gradient at higher rate of heat input. Figure 7 also shows that the computed values of G/R decreases with increasing scanning speed that results from the higher solidification growth rate at higher speed. The constitutional supercooling criterion for plane front solidification is expressed as[27]

$$G/R \geq \Delta T_E/D_L \quad (4)$$

where ΔT_E is the equilibrium solidification temperature range and D_L is the solute diffusion coefficient. The value of ΔT_E for SS316 is 40 K and the carbon diffusivity in liquid iron D_L is about 2×10^{-2} mm^2 s^{-1}.[26] The resulting $\Delta T_E/D_L$ equals to 2×10^3 K s mm^{-2} which is significantly higher than the computed values of G/R for the range of process conditions considered. Thus, Fig. 7 indicates a reduced stability of the plane front and a higher tendency

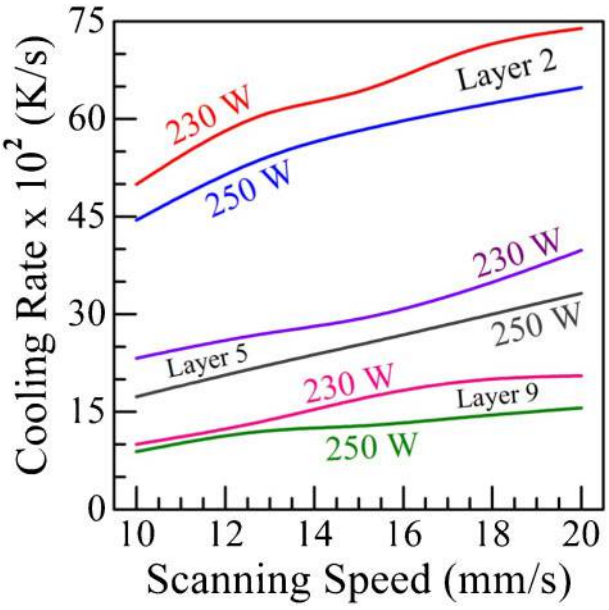

6 Computed cooling rates during solidification (1733–1693 K) for various laser powers and scanning speeds in second, fifth and ninth layers during deposition of 316 stainless steel powder particles

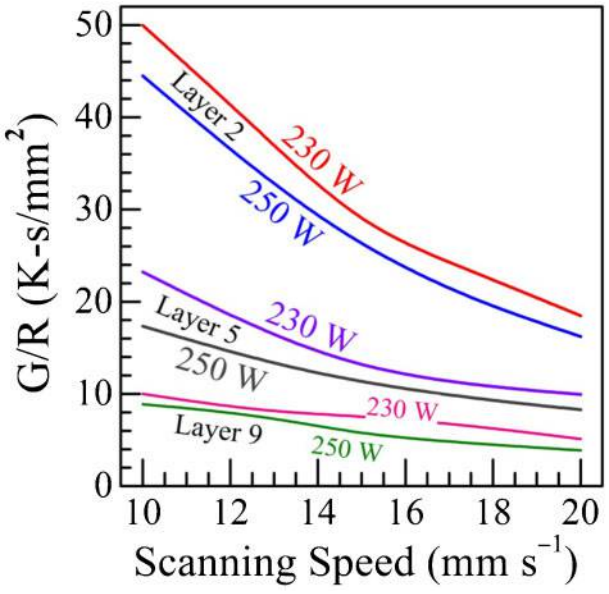

7 Computed values of solidification parameter G/R in melt pool at various laser powers and scanning speeds at second, fifth and ninth layers during deposition of 316 stainless steel

of a cellular or dendritic solidification structure towards the upper layers, which is consistent with the experimentally observed cellular microstructure in similar multilayer deposit in an independent study.[15]

Summary and conclusions

A three-dimensional transient heat transfer and fluid flow model is developed for the laser assisted deposition of a multilayer austenitic stainless steel structure. The computed results of the build geometry, peak temperature and temperature profile are in fair agreement with the corresponding independent experimentally measured results. The computed results show that the peak temperature and melt pool dimensions increase whereas the cooling rate reduces towards upper layers for a specified combination of laser power and scanning speed. The ratio of temperature gradient to solidification growth rate indicates increasing instability of plane front solidification in the upper layers. The computed results also show large velocities of liquid alloy in a small melt pool in the range of 400–600 mm s^{-1}. These large velocities indicate convective heat transfer as the main mechanism of heat transfer within the liquid pool during laser assisted additive manufacturing process.

References

1. M. N. Ahsan, R. Bradley and A. J. Pinkerton: 'Microcomputed tomographyanalysis of intralayer porosity generation in laser direct metal deposition and its causes', *J. Laser Appl.*, 2011, **23**, 022009-1–022009-10.
2. G. P. Dinda, A. K. Dasgupta and J. Mazumder: 'Laser aided direct metal deposition of Inconel 625 superalloy: microstructural evolution and thermal stability', *Mater. Sci. Eng. A*, 2009, **A509**, 98–104.
3. W. Hofmeister, M. Wert, J. Smugeresky, J. Philliber, M. Griffith and M. Ensz: 'Investigating solidification with the laser engineered net shaping (LENS^{TM}) process', *JOMe*, 1999, **51**, (7), available at http://www.tms.org/pubs/journals/jom/9907/hofmeister/hofmeister-9907.html, (accessed 15 August 2014).
4. B. Zheng, Y. Zhou, J. E. Smugeresky, J. M. Schoenung and E. J. Lavernia: 'Thermal behavior and microstructure evolution during laser deposition with laser engineered nest shaping: Part II. Experimental investigation and discussion', *Metall. Mater. Trans. A*, 2008, **39A**, 2237–2245.
5. J. Dutta Majumdar, A. Pinkerton, Z. Liu, I. Manna and L. Li: 'Microstructure characterization and process optimization of laser assisted rapid fabrication of 316L stainless steel', *Appl. Surf. Sci.*, 2005, **247**, 320–327.
6. W. Hofmeister, M. Griffith, M. Ensz and J. Smugeresky: 'Solidification in direct metal depositionby LENS processing', *JOM*, 2001, **53**, 30–34.
7. M. L. Griffith, M. E. Schlienger, L. D. Harwell, M. S. Oliver, M. D. Baldwin, M. T. Ensz, M. Essien, J. Brooks, C. V. Robino, J. E. Smugeresky, W. H. Hofmeister, M. J. Wert and D. V. Nelson: 'Understanding thermal behavior in the LENS process', *Mater. Des.*, 1999, **20**, 107–113.
8. V. K. Balla, W. Xue, S. Bose and A. Bandyopadhyay; 'Laser assisted Zr/ZrO_2 coating on Ti for load-bearing implants', *Acta Biomater.*, 2009, **5**, 2800–2809.
9. W. Liu and J. N. DuPont: '*In-situ* reactive processing of nickel aluminides by laser-engineered net shaping', *Metall. Mater. Trans. A*, 2003, **34A**, 2633–2641.
10. R. Banerjee, A. Genç, D. Hill, P. C. Collin and H. L. Fraser: 'Nanoscale TiB precipitates in laser deposited Ti–matrix composites', *Scr. Mater.*, 2005, **53**, 1433–1437.
11. V. K. Balla, P. P. Bandyopadhyay, S. Bose and A. Bandyapadhyay: 'Compositionally graded yttria-stabilized zirconia coating on stainless steel using laser engineered net shaping (LENS^{TM})', *Scr. Mater.*, 2007, **57**, 861–864.
12. B. Zheng, Y. Zhou, J. E. Smugeresky, J. M. Schoenung and E. J. Lavernia: 'Thermal behavior and microstructural evolution during laser deposition with laser engineered net shaping: Part I. Numerical calculations', *Metall. Mater. Trans. A*, 2008, **39A**, 2228–2236.
13. V. Neela and A. De: 'Three-dimensional heat transfer analysis of LENS^{TM} process using finite element method', *Int. J. Adv. Manuf. Technol.*, 2009, **45**, 935–943.
14. L. Wang and S. Felicelli: 'Process modeling in laser deposition of multilayer SS410 steel', *J. Manuf. Sci. Eng.*, 2007, **129**, 1028–1034.
15. V. D. Manvatkar, A. A. Gokhale, G. Jagan Reddy, A. Venkataramana and A. De: 'Estimation of melt pool dimensions, thermal cycle and hardness distribution in the laser engineered net shaping process of austenitic stainless steel', *Metall. Mater. Trans. A*, 2011, **42A**, 4080–4987.
16. H. Qi, J. Mazumder and H. Ki: 'Numerical simulation of heat transfer and fluid flow in coaxial laser cladding for direct metal deposition', *J. Appl. Phys.*, 2006, **100**, 024903-1–024903-11.
17. X. He and J. Mazumder: 'Transport phenomenon during direct metal deposition', *J. Appl. Phys.*, 2007, **101**, 053113-1–053113-9.
18. S. Wen and Y. C. Shin: 'Modeling of transport phenomena during the coaxial laser direct deposition process', *J. Appl. Phys.*, 2010, **108**, 044908-1–044908-9.
19. F. Kong and R. Kovacevic: 'Modeling of heat transfer and fluid flow in the laser multilayered cladding process', *Metall. Mater. Trans. B*, 2012, **41B**, 1310–1320.
20. S. Morville, M. Carin, P. Peyre, M. Gharbi, D. Carron, P. L. Masson and R. Fabbro: '2D longitudinal modeling of heat transfer and fluid flow during multilayered direct laser metal deposition process', *J. Laser Appl.*, 2012, **24**, 032008-1–032008-9.
21. A. Raghavan, H. L. Wei, T. A. Palmer and T. DebRoy: 'Heat transfer and fluid flow in additive manufacturing', *J. Laser Appl.*, 2013, **25**, 052006-1–52006-8.
22. G. G. Roy, J. W. Elmer and T. DebRoy: 'Mathematical modeling of heat transfer, fluid flow, and solidification during linear welding with a pulsed laser beam', *J. Appl. Phys.*, 2006, **100**, 034903-1–034903-7.
23. A. V. Gusarov and J. P. Kruth: 'Modelling of radiation transfer in metallic powders at laser treatment', *Int. J. Heat Mass Transfer*, 2005, **48**, 3423–3434.
24. K. C. Mills: 'Recommended values of thermophysical properties for selected commercial alloys', 135–146, 2002, Cambridge, Woodhead Publishing Limited.
25. J. Lin: 'Temperature analysis of the powder streams in coaxial laser cladding', *Opt. Laser Technol.*, 1999, **31**, 565–570.
26. V. Manvatkar, A. De and T. DebRoy: 'Heat transfer and material flow during laser assisted multi-layer additive manufacturing', *J Appl. Phys.*, 2014, **116**, 124905.
27. W. Zhang, G. G. Roy, J. W. Elmer and T. DebRoy: 'Modeling of heat transfer and fluid flow during gas tungsten arc spot welding of low carbon steel', *J. Appl. Phys.*, 2003, **93**, 3022–3033.
28. S. V. Patankar: 'Numerical heat transfer and fluid flow'; 1980, Washington, DC, Hemisphere Publishing Corporation.
29. B. Ribic, R. Rai and T. DebRoy: 'Numerical simulation of heat transfer and fluid flow in GTA/laser hybrid welding', *Sci. Technol. Weld. Join.*, 2008, **13**, 683–693.
30. I. Ericsson, J, Powell and F. D. Kaplan: 'Measurements of fluid flow on keyhole front during laser welding', *Sci. Technol. Weld. Join.*, 2011, **16**, 636–641.